



CHORUS

This is the accepted manuscript made available via CHORUS. The article has been published as:

Electrochemical-Reaction-Driven Interfacial Stress in a Solid-Solid Layered Architecture

Feng Hao, Wenxiu Wang, and Partha P. Mukherjee

Phys. Rev. Applied **11**, 034038 — Published 15 March 2019

DOI: [10.1103/PhysRevApplied.11.034038](https://doi.org/10.1103/PhysRevApplied.11.034038)

**Electrochemical Reaction Driven Interfacial Stress in a Solid/Solid
Layered Architecture**

Feng Hao, Wenxiu Wang, and Partha P. Mukherjee*

School of Mechanical Engineering, Purdue University, West Lafayette, IN 47907, USA

Revised manuscript submitted to

Physical Review Applied

January 2019

*Correspondence: pmukherjee@purdue.edu

Abstract

Reaction driven interfacial growth causes significant strain in layered architectures accompanied by mass transfer and moving boundaries. Here, we present an analytical construct of the stress generated in a multi-layer film which incorporates the elastic-plastic strain of the growth layer, which suggests its strong dependence on the mechanical properties and thickness. This analytical formalism is further applied to a layered all-solid-state lithium battery architecture. This study demonstrates that mechanical stability can be enhanced by using a positive electrode material with high stiffness, porous hosts for lithium plating, and small external elastic constraints to buffer the volumetric changes in the electrode material. Our results also reveal that small surface flaws in the solid electrolyte and high internal hydrostatic pressure can alleviate lithium dendrite growth through surface cracks.

Keywords: Interfacial growth, multilayer film, all-solid-state Li battery, stress, fracture

I. INTRODUCTION

Layered, functional architectures have attracted intensive research interest, in emerging engineering applications, such as flexible electronics [1], gas separation [2], and energy storage [3]. The thickness of multilayer film could range from a few nanometers to millimeters, such as heteroepitaxial superlattice, coating, and laminated composite. In practical applications, each layer plays a unique role for special functions [4-6]. The damage of one layer could result in part or even catastrophic failure of the multilayer film. For batteries, the fracture of electrode exacerbates capacity fade, while the damage of separator could cause short circuit and explosion.

Mechanical stability is of great significance to ensure the robust performance of multilayer film. Under the operating conditions, multilayer films could be subject to large stresses, which leads to the failure of the film. Therefore, many efforts have been made to model the stress and reveal the failure mechanisms [7,8], including material fracture and film buckling. For instance, given that the interface was susceptible to environmentally-assisted subcritical debonding, the interfacial fracture resistance was quantitatively measured [9]. Theoretical models were developed to study the thermal stress in multilayer thin films, which provided guidance on the physical design of layered electronics [10,11]. The mechanics of ridge-cracked buckle delamination for compressed multilayers on curved substrates was established, which was applied to thermal barrier systems [12].

Physicochemical reactions could occur at the interfaces in a multilayer film, such as interfacial corrosion and metal electrodeposition, resulting in a new growth layer. In

the presence of the new interfacial layer, the initial stress field will be significantly changed in the confined space. For instance, multilayer films are used in energy storage systems [13], for example in all-solid-state lithium batteries, which have the layered structure of negative electrode, solid electrolyte separator, and positive electrode. In addition to the interfacial metal electrodeposition, the mass transfer also causes volumetric changes in electrodes. Recently, stresses were experimentally measured for all-solid-state batteries [14]. However, previous studies primarily focused on diffusion induced stresses at the electrode level [15-17], while the mechanics needs to be established for the novel multilayer film, which involves interfacial growth between different layers.

To this end, we first develop a simple theoretical model to analytically obtain the stresses in multilayer film, which stems from the interfacial growth layer and mass transfer. The elastic-plastic strain of the growth layer is considered. As an application, the developed model is used to investigate the mechanisms of Li plating induced stress in all-solid-state Li metal battery, which mainly consists of a layered structure of lithium metal, solid electrolyte separator, and a positive electrode film [18,19]. Mechanical failure is one of the critical degradation mechanisms of Li-ion batteries [20]. Based on our model, strategies are proposed which can facilitate releasing the interfacial build-up and avoid crack formation in the positive electrode and solid electrolyte. This study provides fundamental understanding of lithium plating induced stress in an all-solid-state Li metal battery, and suggests potential strategies to buffer volume changes in the electrode solid electrolyte and electrode layers which could

potentially avoid mechanical failures.

II. INTERFACIAL GROWTH INDUCED STRESS IN A LAYERED ARCHITECTURE

Linear elastic analysis

Fig. 1 illustrates a layered structure, comprised of N film layers. Due to the driving force, species (named A below) escape from the reservoir of the N th film and transport across the layered structure. Upon the arrival at the interface between Layer 1 and Layer 2, A is deposited under chemical (electrochemical) reactions or physical adsorption, leading to the formation of Layer 0. Because of the transfer of A , the multilayer film significantly undergoes volume changes, which originate from two parts: contraction of Layer N and expansion of Layer 0. As the release of A from the reservoir continues, the N th layer is gradually shrunk. Conversely, the thickness of Layer 0 increases during A deposition. Consequently, the volume changes produce built-in stresses across the system.

Here, the three directions are denoted by x , y , and z , with y in the direction normal to the film (thickness direction). Layers are assumed to be well contacted during A transfer, without the interfacial slip and delamination. As a result, there are no shear stresses, and the three principal stresses are σ_{xx} , σ_{yy} , and σ_{zz} .

First, we assume that all the materials experience elastic deformations. In the regime of isotropic linear elasticity, the constitutive equations read

$$\varepsilon_{ij} = -\frac{\nu}{E} \sigma_{kk} \delta_{ij} + \frac{1+\nu}{E} \sigma_{ij}. \quad (1)$$

ε_{ij} is the strain tensor and σ_{ij} is the stress tensor. δ_{ij} is the Kronecker delta. All the indices run from x to z , corresponding to the three directions, and the repeated index k implies summation. E is the Young's modulus and ν is the Poisson's ratio.

For the N th layer, the constitutive equations are revised as [21]

$$\varepsilon_{ij} = -\frac{\nu}{E} \sigma_{kk} \delta_{ij} + \frac{1+\nu}{E} \sigma_{ij} - \varepsilon_0 \delta_{ij}. \quad (2)$$

where the last term ε_0 is the eigenstrain, accounting for the volume shrinkage after the release of A from the N th layer, which is expressed by

$$\begin{aligned} \varepsilon_0 &= (V_c + 1)^{\frac{1}{3}} - 1, \\ V_c &= \frac{V_0 - V}{V_0} = (c_0 - c) \Omega_N, \end{aligned} \quad (3)$$

where V_c represents the volume strain. V_0 is the reference volume of the N th film and V is the current volume. c is the concentration in the N th layer, c_0 is the reference concentration, and Ω_N is the partial molar volume of A in the N th layer.

Given that the thickness of each layer is much smaller than the sizes in the other two directions, the strains in the directions x and z are neglected, which is similar to the case of plane strain. Thus, we have

$$\varepsilon_{xx} = \varepsilon_{zz} = 0, \quad (4)$$

$$\sigma_{xx} = \sigma_{zz}. \quad (5)$$

Substituting Eqs. (5) into Eqs. (1) and (2) separately, and then using Eq. (4), we can get

$$\sigma_{xx} = \sigma_{zz} = \frac{\nu}{1-\nu} \sigma_{yy}, \quad (6)$$

$$\sigma_{xx} = \sigma_{zz} = \frac{\nu}{1-\nu} \sigma_{yy} + \frac{1}{1-\nu} E \varepsilon_0, \quad (7)$$

Eq. (6) is valid for Layer 0 to Layer $N-1$, and Eq. (7) is for the N th layer. Substituting

the two equations back into Eqs. (1) and (2), respectively, we obtain

$$\varepsilon_{yy} = \frac{(1-2\nu)(1+\nu)}{E(1-\nu)} \sigma_{yy}, \quad (8)$$

$$\varepsilon_{yy} = \frac{(1-2\nu)(1+\nu)}{E(1-\nu)} \sigma_{yy} - \frac{1+\nu}{1-\nu} \varepsilon_0. \quad (9)$$

Hence, the derived constitutive equations concisely relate the strain to the stress in the y -axis direction.

Due to the reactions at the interface between the first two layers, the transfer of A from the N th layer leads to a moving reaction front. The increased thickness at the interface is given as

$$l_0 = \frac{(c_0 - c)V_0\Omega_A}{S} = (c_0 - c)\Omega_A l_N = \frac{\Omega_A}{\Omega_N} V_c l_N, \quad (10)$$

where V_0 , S , and l_N are the volume, cross-sectional area, and thickness of the N th layer, respectively, and Ω_A is the molar volume of substance A .

In the y -axis direction, the total thickness of the system is assumed to be constant, which satisfies that

$$l_0 + \varepsilon_{yyi} l_i + \Delta l_{N+1} = 0, \quad (11)$$

where i runs from 0 to N , l_i is the thickness of Layer i , ε_{yyi} is the y -axis strain of Layer i , and Δl_{N+1} denotes the thickness change of other surrounding components. We have that $\Delta l_{N+1} = F/k = \sigma_{yy} S/k = \sigma_{yy} / (k/S) = \sigma_{yy} / K$, where F is the total force in the thickness direction, k is the effective spring constant applied to the layered structure from the surroundings, and S is the effective area. Thus, K is interpreted as the effective stiffness per area (the required stress under the thickness change of 1 μm), which could be affected by other battery components, such as the current collector, internal spring, metal shell, etc. If the multilayer film is subject to rigid constraints, Δl_{N+1} is equal to

zero. Note also that each layer has the same stress in the thickness direction

$$\sigma_{yy} = \sigma_{yyi}. \quad (12)$$

Upon the substitution of Eqs. (8), (9), and (12) into Eq. (11), the stress in the thickness direction is solved as

$$\sigma_{yy} = \left[\sum_{i=0}^N \frac{(1-2\nu_i)(1+\nu_i)}{E_i(1-\nu_i)} l_i + \frac{1}{K} \right]^{-1} \left(\frac{1+\nu_N}{1-\nu_N} \varepsilon_0 l_N - l_0 \right). \quad (13)$$

Subsequently, the stresses in the x -axis and y -axis directions can be obtained by Eqs. (6) and (7).

In the multilayer film, releasing stress can avert structural failures. An ideal condition is that the stress in the thickness direction is zero, which requires that the expansion of the interface layer is well compensated by the contraction of the N th layer.

From Eq. (13), it is evident that

$$\frac{1+\nu_N}{1-\nu_N} \varepsilon_0 l_N - l_0 = 0. \quad (14)$$

Using Eqs. (3) and (10), the above equality is rephrased as

$$\frac{\Omega_A}{\Omega_N} = \frac{1+\nu_N}{1-\nu_N} \frac{1}{V_c} \left[(V_c + 1)^{\frac{1}{3}} - 1 \right]. \quad (15)$$

On the right hand, ν_N and V_c are both physical parameters of the N th film. If V_c is infinitesimal (compared to 1), Eq. (15) is reduced to

$$\frac{\Omega_A}{\Omega_N} = \frac{1+\nu_N}{3(1-\nu_N)}. \quad (16)$$

In essence, no stress is produced in the thickness direction if the material parameters satisfy Eq. (15). Fig. 2 illustrates the map of Ω_A / Ω_N in terms of the

Poisson's ratio and the volume strain of the N th layer. It can be seen that regardless of ν_N and V_c , Ω_A / Ω_N is always less than one.

Elastic-plastic analysis

If A is a ductile material, for instance metal, the interfacial growth layer will experience plastic deformation when stress reaches its initial yield strength. Therefore, the elastic-plastic behavior needs to be taken into account. In the following, we assume that Layer 0 and Layer 1 have the same ductile material A , and other layers are brittle materials. For Layer 1 (Layer 0 included), Eq. (1) is rewritten as

$$\varepsilon_{ij1} = -\frac{\nu_1}{E_1} \sigma_{kk1} \delta_{ij} + \frac{1+\nu_1}{E_1} \sigma_{ij1} + \varepsilon_{ij1}^p. \quad (17)$$

The strain tensor is decomposed into elastic and plastic parts, where the last term is the plastic strain. Given that plastic deformation does not affect the volume change, we have [22]

$$\varepsilon_{xx1}^p + \varepsilon_{yy1}^p + \varepsilon_{zz1}^p = 0, \quad (18)$$

where ε_{xx1}^p , ε_{yy1}^p , and ε_{zz1}^p are the three components of plastic strain in the three directions. Set that the plastic strain in the film thickness direction is ε^p , we can get $\varepsilon_{yy1}^p = \varepsilon^p$ and $\varepsilon_{xx1}^p = \varepsilon_{zz1}^p = -\varepsilon^p / 2$. In view of Eqs. (4), (5), and (17), it gives

$$\frac{1}{E_1} \left[(1-\nu_1) \sigma_{xx1} - \nu_1 \sigma_{yy1} \right] - \frac{1}{2} \varepsilon^p = 0, \quad (19)$$

$$\frac{1}{E_1} (\sigma_{yy1} - 2\nu_1 \sigma_{xx1}) + \varepsilon^p = \varepsilon_{yy1}. \quad (20)$$

To solve the stress, we need one more equation, namely the yield criterion.

For a ductile material, von Mises criterion is the most frequently utilized yield

criterion [22], which takes the form

$$J_2 = \frac{1}{2} s_{ij} s_{ij} = k^2. \quad (21)$$

k is the material parameter, which is a function of plastic deformation history. J_2 is the second invariant of the deviatoric part of stress tensor s_{ij} , which is defined as

$s_{ij} = \sigma_{ij} - \sigma_{kk} \delta_{ij} / 3$. In terms of the principal stresses in Layer 1, J_2 is expressed as

$$J_2 = \frac{1}{6} \left[(\sigma_{xx} - \sigma_{yy})^2 + (\sigma_{yy} - \sigma_{zz})^2 + (\sigma_{zz} - \sigma_{xx})^2 \right]. \quad (22)$$

In general, uniaxial tension is used to obtain $k(\bar{\varepsilon}^p)$, where $\bar{\varepsilon}^p$ is the effective plastic strain. From the stress-strain curve, the yield stress is deduced as a function of plastic strain: $\bar{\sigma}(\bar{\varepsilon}^p)$. We have

$$k = \frac{\bar{\sigma}(\bar{\varepsilon}^p)}{\sqrt{3}}. \quad (23)$$

For Layer 1, the stress state is different from uniaxial tension. Using $\varepsilon_{yy1}^p = \varepsilon^p$ and $\varepsilon_{xx1}^p = \varepsilon_{zz1}^p = -\varepsilon^p / 2$ for the current case, the effective plastic strain is given as

$$\bar{\varepsilon}^p = \int_0^t \left(\frac{2}{3} D_{ij}^p D_{ij}^p \right)^{1/2} dt = \int \left(\frac{2}{3} d\varepsilon_{ij}^p d\varepsilon_{ij}^p \right)^{1/2} = |\varepsilon^p|, \quad (24)$$

where D_{ij}^p is the plastic rate of deformation. As a result, if Layer 1 is compressed ($\sigma_{yy1} < 0$), the effective plastic strain is equal to the opposite of the plastic strain in the thickness direction. When Eqs. (22) and (23) are incorporated into Eq. (21), it follows that

$$(\sigma_{yy1} - \sigma_{xx1})^2 = \bar{\sigma}^2(\bar{\varepsilon}^p) = \bar{\sigma}^2(|\varepsilon^p|). \quad (25)$$

Combining Eqs. (19) with (25) and then using Eq. (20), we can finally establish the relation between ε_{yy1} and σ_{yy1} with the effect of plasticity in Layer 1. Nevertheless, the relation depends on the yield stress $\bar{\sigma}(\bar{\varepsilon}^p)$ measured in uniaxial tension.

For simplicity, linear isotropic hardening model is used. Therefore, we assume that the stress-strain curve in uniaxial tension has two linear parts. After stress exceeds the initial yield stress, the new yield stress is expressed as

$$\bar{\sigma} = E^0 \left(\bar{\varepsilon} - \frac{\sigma_s}{E} \right) + \sigma_s. \quad (26)$$

E is the Young's modulus, E^0 is the tangent modulus (slope) after the initial yield, and σ_s is the initial yield stress. Strain $\bar{\varepsilon}$ is the sum of elastic and plastic parts, i.e.

$$\bar{\varepsilon} = \frac{\bar{\sigma}}{E} + \bar{\varepsilon}^p. \quad (27)$$

The substitution of Eq. (27) into Eq. (26) gives

$$\bar{\sigma} = \frac{EE^0}{E-E^0} \bar{\varepsilon}^p + \sigma_s. \quad (28)$$

$EE^0/(E-E^0)$ is physically interpreted as the plastic modulus.

Thus, Eq. (19) is rewritten as

$$\sigma_{xx1} = \left[1 + \frac{2E_1^0}{E_1 - E_1^0} (1 - \nu_1) \right]^{-1} \left[\left(1 + \frac{2E_1^0}{E_1 - E_1^0} \nu_1 \right) \sigma_{yy1} + \sigma_s^0 \right], \quad (29)$$

where

$$\sigma_s^0 = \begin{cases} \sigma_s, & \sigma_{yy1} < 0 \\ -\sigma_s, & \sigma_{yy1} > 0 \end{cases}. \quad (30)$$

The substitution of Eqs. (19) and (29) into (20) yields

$$\begin{aligned} \varepsilon_{yy1} = & \frac{1-2\nu_1}{E_1} \left\{ 2 \left(1 + \frac{2E_1^0}{E_1 - E_1^0} \nu_1 \right) \left[1 + \frac{2E_1^0}{E_1 - E_1^0} (1 - \nu_1) \right]^{-1} + 1 \right\} \sigma_{yy1} \\ & + 2 \frac{1-2\nu_1}{E_1} \left[1 + \frac{2E_1^0}{E_1 - E_1^0} (1 - \nu_1) \right]^{-1} \sigma_s^0. \end{aligned} \quad (31)$$

Similar to the procedure used to obtain Eq. (13), the stress in the thickness direction is solved as

$$\sigma_{yy} = C_1 \left[\frac{1}{C_2} (l_1 + l_0) + \sum_{i=2}^N \frac{(1-2\nu_i)(1+\nu_i)}{E_i(1-\nu_i)} l_i + \frac{1}{K} \right]^{-1}, \quad (32)$$

where

$$C_1 = \frac{1+\nu_3}{1-\nu_3} \varepsilon_0 l_3 - l_0 - 2 \frac{1-2\nu_1}{E_1} \left[1 + \frac{2E_1^0}{E_1 - E_1^0} (1-\nu_1) \right]^{-1} \sigma_s^0 (l_1 + l_0), \quad (33)$$

$$\frac{1}{C_2} = \frac{1-2\nu_1}{E_1} \left\{ 2 \left(1 + \frac{2E_1^0}{E_1 - E_1^0} \nu_1 \right) \left[1 + \frac{2E_1^0}{E_1 - E_1^0} (1-\nu_1) \right]^{-1} + 1 \right\}. \quad (34)$$

Correspondingly, other stresses can be analytically solved by using constitutive equations. If non-linear isotropic hardening is assumed, a non-linear relationship between $\bar{\sigma}$ and $\bar{\varepsilon}$ will be presented in Eq. (26). The stress in the thickness direction σ_{yy} could also be obtained by numerical calculations.

III. APPLICATION TO ALL-SOLID-STATE LI BATTERY

The model is applied to all-solid-state Li battery, of which the multilayer film is comprised of the Li metal film (Layer 1), solid electrolyte separator (Layer 2), and positive electrode film (Layer 3). Li-ions diffuse out of the positive electrode film and transport across the solid electrolyte separator. Upon the arrival at the solid electrolyte-Li interface, Li-ions are reduced and then deposited on the negative electrode surface. As the deintercalation of Li-ions from the positive electrode continues, the positive electrode film is gradually shrunk. Conversely, the thickness of Li metal increases during Li plating.

For Li metal, the molar volume is $1.3 \times 10^{-5} \text{ m}^3 \text{ mol}^{-1}$ [23,24]. If the positive electrode material is LiMn_2O_4 , the partial molar volume of Li-ion is $3.5 \times 10^{-6} \text{ m}^3 \text{ mol}^{-1}$

¹ [25]. Obviously, Eq. (15) does not hold for the use of LiMn₂O₄. For Li₂S, the electrochemical reactions are



When the reaction proceeds from the left to the right, the volume contraction of Li₂S is about 44%. Considering that the molar volumes of S₈ and Li₂S are $1.239 \times 10^{-4} \text{ m}^3 \text{ mol}^{-1}$ and $2.768 \times 10^{-5} \text{ m}^3 \text{ mol}^{-1}$ [26], the partial molar volume of Li-ion in Li₂S is readily calculated as $6.1 \times 10^{-6} \text{ m}^3 \text{ mol}^{-1}$. Thus, Eq. (15) does not hold. For conventional positive electrodes, such as LiCoO₂, LiMn₂O₄, and LiFePO₄, the Poisson's ratio ranges from 0.24 to 0.32, and the volume strain ranges from 2% to 6.8% [27]. For the positive electrode Li₂S, the volume strain is 44% when Li₂S is oxidized to S during Li plating on the negative electrode. Thus, the Poisson's ratios and volume strains of most positive electrodes are within the ranges considered in Fig. 2. For Li metal film, Eq. (15) could not be satisfied because of the relatively larger molar volume of Li compared with the partial molar volumes of Li-ion in common positive electrode materials. As a result, stresses are generated in the layered film.

In the regime of elasticity, stress is given by Eq. (13). However, Li metal experiences both elastic and plastic deformations when the yield criterion in Eq. (21) is satisfied. If Li metal is considered as a linear isotropic hardening material, stress is analytically solved in Eq. (32). The solid electrolytes and electrodes are assumed to be homogeneous. Considering Li-oxides on Li metal is much thinner than the metal electrode, their influences on the mechanics of our model are neglected. Unless otherwise indicated, we use the material parameters listed in Table 1 [10,23,25,28,29],

with $\text{Li}_2\text{S-P}_2\text{S}_5$ used as the solid electrolyte, and set that $l_1 = 10 \text{ }\mu\text{m}$, $l_2 = 25 \text{ }\mu\text{m}$, $l_3 = 70 \text{ }\mu\text{m}$, and $K_4 = 50 \text{ MPa um}^{-1}$.

Table 1. Material Parameters

Parameters		Li	Solid electrolyte	Positive electrode	Units
E	Young's modulus	1.9	20	10	GPa
ν	Poisson's ratio	0.42	0.3	0.3	
σ_s	Initial yield stress	0.53			MPa
E^0	Tangent modulus ($\sigma > \sigma_s$)	17.1			MPa
Ω	(Partial) Molar volume	1.3×10^{-5}		4.5×10^{-6}	$\text{m}^3 \text{ mol}^{-1}$
V_c	Volume strain			0.05	

Fig. 3 shows the three principal stresses of the positive electrode, solid electrolyte separator, and Li metal. Because the thickness increase of Li metal is larger than the thickness decrease of the positive electrode film, the multilayered structure is prone to expansion, leading to a compressive stress in the thickness direction. As Li plating proceeds, the growing Li generates a larger compressive stress σ_{yy} . In the x -axis and z -axis directions, Li metal and solid electrolyte separator are also subject to compressive stresses. For Li metal film, the curves of the three principal stresses almost overlap when Li plasticity is considered, producing a triaxial compressive stress state. In contrast, the solid electrolyte separator has relatively smaller compressive stresses σ_{xx} and σ_{zz} in comparison to σ_{yy} . Based on our results, solid electrolytes undergo stress in the confined space of all-solid-state batteries, and the stress could affect ionic transport

in the solid electrolytes, as demonstrated in previous studies [30,31]. Thus, further efforts are needed to examine the roles of stress on ionic conduction of solid electrolytes and battery performance. For the positive electrode film, tensile stresses are generated in the xz plane as opposed to the compressive stress in the thickness direction. The stretching effect is due to the contribution from the delithiation-induced eigenstrain ε_0 in the positive electrode, as shown in Eq. (7).

Fig. 3(b) shows the stress difference $\sigma_{xx1} - \sigma_{yy}$ of Li metal in the early Li plating. Obviously, there are two stages. Li metal film deforms elastically when V_i/V_c is extremely small. As the stress difference exceeds the initial yield stress of 0.53 MPa, the material begins to yield, leading to elastic-plastic deformations. Owing to the plastic strain hardening, the yield strength linearly increases. Therefore, the stress difference gradually increases with growing Li metal thickness.

Next, the influences of material parameters on stress are examined. For Eq. (13) or (32), we can define

$$\frac{1}{K_1} = \frac{(1-2\nu_1)(1+\nu_1)}{E_1(1-\nu_1)}l_1, \quad \frac{1}{K_2} = \frac{(1-2\nu_2)(1+\nu_2)}{E_2(1-\nu_2)}l_2, \quad \frac{1}{K_3} = \frac{(1-2\nu_3)(1+\nu_3)}{E_3(1-\nu_3)}l_3. \quad (36)$$

K_1 , K_2 , and K_3 are the elastic stiffness coefficients of the Li metal film, solid electrolyte separator, and positive electrode film, respectively, which are a combination of mechanical properties and thickness. In the following, K_3 is varied by changing the Young's modulus of the positive electrode, and K_4 is also varied. For Li metal and solid electrolyte, the material parameters remain the same as those in Table 1.

Fig. 4(a) shows the stress difference σ_{yy} in terms of K_3/K_1 and K_4/K_1 . The

compressive stress σ_{yy} increases with increasing K_3/K_1 and K_4/K_1 . In contrast, Fig. 3(b) show a different map for the stress $\sigma_{xx3}(\sigma_{zz3})$ of the positive electrode film. σ_{xx3} increases with increasing K_3/K_1 and decreasing K_4/K_1 . Interestingly, as K_3/K_1 decreases, σ_{xx3} can be transitioned from tensile stress to compressive stress. In Eq. (7), the competition between the two terms on the right hand governs the value of σ_{xx3} . The first term is negative, while the second term is positive. As the Young's modulus of the positive electrode decreases, the values of the two terms both decreases. However, the decrease of the second term is larger than that of the first term, which eventually results in a compressive stress.

For Li metal, plastic deformation occurs when the von Mises criterion is satisfied. On the other side, the materials in other layers are considered as brittle materials, and the fracture is assumed to obey the maximum shear stress criterion [22]

$$\frac{1}{2} \max(|\sigma_{xx} - \sigma_{yy}|, |\sigma_{yy} - \sigma_{zz}|, |\sigma_{zz} - \sigma_{xx}|) = \sigma_F, \quad (37)$$

Where σ_F is the critical stress.

By using the criterion, Figs. 5(a) and (b) show the phase maps of mechanical stability for the positive electrode and solid electrolyte separator, respectively, where the yield stress is assumed to be 1.5 percent of Young's modulus in this study, $\sigma_F = 0.015 E$. The blue represents safe zone and the white denotes failure zone. For a fixed K_3/K_1 , reducing K_4/K_1 is beneficial to the mechanical stability of the positive electrode. Inversely, for a fixed K_4/K_1 , increasing K_3/K_1 can avoid the failure of the positive electrode film. In Fig. 5(b), the solid electrolyte separator fails under the conditions that both K_3/K_1 and K_4/K_1 are large. In addition, Fig. 5(c) shows the combined phase map,

where the blue indicates the shared safe zone for the positive electrode film and solid electrolyte separator. K_4/K_1 is less than 1.75 in the safe zone, which indicates that the constraint on the layered structure should be weak. In Fig. 5(d), the stress difference $\sigma_{xx} - \sigma_{yy}$ of Li metal is illustrated. If K_4/K_1 is very small, Li metal only experiences elastic deformation during Li plating, since the large volume changes of electrode films are buffered by the surroundings.

In the above analysis, Li is electrodeposited on Li metal, and thus, Ω_{Li} is set to $1.3 \times 10^{-5} \text{ m}^3 \text{ mol}^{-1}$ [23]. If Li is deposited into porous hosts [32], the volume change will be significantly reduced, leading to a smaller Ω_{Li} . Therefore, the effect of Ω_{Li} on stress is studied, as shown in Fig. 6. Three specific cases are chosen: $K_3/K_1 = 1$ and $K_4/K_1 = 0.05$, $K_3/K_1 = 1$ and $K_4/K_1 = 0.5$, and $K_3/K_1 = 4$ and $K_4/K_1 = 2$. With varying $\Omega_{Li} / \Omega_{Li^+}$, the three cases are denoted by the black, red, and blue lines in Fig. 6, respectively. It can be seen that as $\Omega_{Li} / \Omega_{Li^+}$ decreases, the failures of the positive electrode film and solid electrolyte separator does not occur when $(\sigma_{xx} - \sigma_{yy}) / 2\sigma_F$ is reduced below one in Fig. 6(a). For porous hosts, Ω_{Li} is allowed to be smaller than Li molar volume. Fig. 6(b) demonstrated that there is no stress generated in the thickness direction when Eq. (16) is satisfied (V_c is 0.05, much smaller than 1.0). As $\Omega_{Li} / \Omega_{Li^+}$ continues to decrease, the thickness reduction of the positive electrode film is less than the thickness increase of Li, thereby causing a tensile stress of σ_{yy} .

In addition, Li dendrite growth can produce local stresses and electrochemical potential changes, which induce crack propagation and even short circuit. Li dendrite could penetrate the solid electrolyte separator through the surface flaws of solid

electrolytes, like surface pre-existing cracks and grain boundaries [33]. Here, the edge crack model is used to simplify the problem. In Fig. (7), the green is the solid electrolyte, the white is a surface crack, and the gray is Li dendrite. At the dendrite-electrolyte interface (crack surface), Li-ions are reduced, and the electrodeposited Li atoms can diffuse over the dendrite surface (the dashed line). Because of the expansion of Li dendrite inside the crack, we assume that the crack is subject to a uniformly distributed pressure of p . As the pressure increases, the crack-tip could be forced to advance, thereby favoring the dendrite growth through the solid electrolyte separator.

Considering the stress σ_{xx2} in the vertical direction, the stress intensity factor is given by [34]

$$K_I = 1.12(p - |\sigma_{xx2}|)\sqrt{\pi a}. \quad (38)$$

Here, σ_{xx2} is negative. The crack growth requires that

$$K_I \geq K_{Ic}, \quad (39)$$

where K_{Ic} is the fracture toughness of solid electrolyte, which can be measured from experiments. For $\text{Li}_2\text{S-P}_2\text{S}_5$ (LPS) and $\text{Li}_7\text{La}_3\text{Zr}_{12}\text{O}_{12}$ (LLZO), K_{Ic} are 0.23 and 1.25 MPa $\text{m}^{1/2}$, respectively [35,36]. Fig. 7 illustrates the crack length dependent critical stress that causes the crack propagation and thus Li dendrite growth. Based on Fig. 7, there are three strategies to alleviate Li dendrite penetration through solid electrolytes.

Compared with LPS, LLZO has a higher critical stress due to its relatively larger fracture resistance. Therefore, enhancing the fracture toughness of solid electrolyte helps to suppress Li dendrite growth through the solid electrolyte separator. Increasing fracture toughness contributes to the suppression of Li dendrite growth through solid

electrolytes, however, it could also cause the reduction in ionic conductivity [38], which also applies to the comparison of LPS and LLZO. Thus, a trade-off could exist for the use of solid electrolytes with high fracture toughness, and a balance is needed to achieve high performance of all-solid-state batteries. The size of surface flaw plays a key role in determining the crack opening. The critical stress is significantly reduced with increasing length of surface flaw, and thus, the crack can propagate under a lower pressure from Li dendrite. In turn, the growing dendrite fills the void of new crack. To avoid the crack growth, we can reduce the density and size of surface defects, such as polishing the separator surface and coating the separator with a dense and defect-free layer. In addition, it can be seen that the pressure p , originating from Li dendrite expansion, needs to overcome the stress σ_{xx2} for the crack growth. In literature, applying a pressure inside the battery was reported as an effective method to improve Li electrodeposition [37].

IV. CONCLUSION

In summary, we develop a theoretical model of interfacial growth induced stress in the multilayer film, which enables us to analytically obtain the stresses. In this model, the elastic-plastic deformation of the growth layer is considered. The model demonstrates that stresses largely depend on the elastic properties and thicknesses of all the layers in the system. A concise formula is deduced for a particular case that no stress is produced in the film thickness direction. The model is applied to investigate the mechanical behaviors of the layered structure of Li metal-separator-positive

electrode in all-solid-state battery. Based on our results, we can draw the conclusions as follows. (1) In the early stage of Li plating, the Li metal electrode undergoes elastic deformation. To avoid the failure of materials, the positive electrode film needs to have high stiffness, and the external elastic constraints on the multilayer film should be small to release the volumetric changes of electrode materials. (2) Stress can be significantly reduced by using porous hosts for Li electrodeposition due to relatively low Li molar volume. In practice, porous hosts could also increase the active sites and thus avoid Li dendrite growth at high current density. (3) Dendrite growth in the solid electrolyte is also analyzed. It is found that Li dendrite penetration through the solid electrolyte separator can be alleviated by increasing the fracture toughness of solid electrolytes, reducing surface flaw size, and applying internal battery pressure. In practical applications, Li^+ migration through solid electrolytes is driven by the gradient of the chemical potential, which could be affected by local defects. Thus, a mechanistic study is needed to explore the role of defects on Li^+ migration. In addition, a coupled model of mechanics-electrochemistry will be developed to understand the interactions between stress and Li^+ migration in our future work.

ACKNOWLEDGEMENT

The information, data, or work presented herein was funded in part by the Office of Energy Efficiency and Renewable Energy (EERE), U.S. Department of Energy, under Award DE-EE0007766, and Purdue University faculty research grant.

References

- [1] S.-H. Bae, O. Kahya, B. K. Sharma, J. Kwon, H. J. Cho, B. Özyilmaz, and J.-H. Ahn, Graphene-P(VDF-TrFE) Multilayer Film for Flexible Applications, *ACS Nano* **7**, 3130 (2013).
- [2] H. W. Kim *et al.*, Selective Gas Transport Through Few-Layered Graphene and Graphene Oxide Membranes, *Science* **342**, 91 (2013).
- [3] M. M. Lee, J. Teuscher, T. Miyasaka, T. N. Murakami, and H. J. Snaith, Efficient Hybrid Solar Cells Based on Meso-Superstructured Organometal Halide Perovskites, *Science* **338**, 643 (2012).
- [4] B. Van Troeye, A. Lherbier, J.-C. Charlier, and X. Gonze, Large phosphorene in-plane contraction induced by interlayer interactions in graphene-phosphorene heterostructures, *Phys. Rev. Mater.* **2**, 074001 (2018).
- [5] S. Choi *et al.*, Correlation of Fe-Based Superconductivity and Electron-Phonon Coupling in an FeAs/Oxide Heterostructure, *Phys. Rev. Lett.* **119**, 107003 (2017).
- [6] J. Fischer *et al.*, Spin Hall magnetoresistance in antiferromagnet/heavy-metal heterostructures, *Phys. Rev. B* **97**, 014417 (2018).
- [7] A. K. Noor and W. S. Burton, Assessment of Shear Deformation Theories for Multilayered Composite Plates, *Appl. Mech. Rev.* **42**, 1 (1989).
- [8] S. Li, J. Wang, and M. D. Thouless, The effects of shear on delamination in layered materials, *J. Mech. Phys. Solids* **52**, 193 (2004).
- [9] R. H. Dauskardt, M. Lane, Q. Ma, and N. Krishna, Adhesion and debonding of multi-layer thin film structures, *Eng. Fract. Mech.* **61**, 141 (1998).
- [10] E. Suhir, An Approximate Analysis of Stresses in Multilayered Elastic Thin Films, *J. Appl. Mech.* **55**, 143 (1988).
- [11] Z. Q. Jiang, Y. Huang, and A. Chandra, Thermal Stresses in Layered Electronic Assemblies, *J. Electron. Packaging* **119**, 127 (1997).
- [12] S. Faulhaber, C. Mercer, M. W. Moon, J. W. Hutchinson, and A. G. Evans, Buckling delamination in compressed multilayers on curved substrates with accompanying ridge cracks, *J. Mech. Phys. Solids* **54**, 1004 (2006).
- [13] J. W. Choi and D. Aurbach, Promise and reality of post-lithium-ion batteries with high energy densities, *Nat. Rev. Mater.* **1**, 16013 (2016).
- [14] R. Koerver *et al.*, Chemo-mechanical expansion of lithium electrode materials – on the route to mechanically optimized all-solid-state batteries, *Energy Environ. Sci.* **11**, 2142 (2018).
- [15] H. Haftbaradaran, X. Xiao, M. W. Verbrugge, and H. Gao, Method to deduce the critical size for interfacial delamination of patterned electrode structures and application to lithiation of thin-film silicon islands, *J. Power Sources* **206**, 357 (2012).

- [16] G. Bucci, S. P. V. Nadimpalli, V. A. Sethuraman, A. F. Bower, and P. R. Guduru, Measurement and modeling of the mechanical and electrochemical response of amorphous Si thin film electrodes during cyclic lithiation, *J. Mech. Phys. Solids* **62**, 276 (2014).
- [17] F. Hao and P. P. Mukherjee, Mesoscale Analysis of the Electrolyte-Electrode Interface in All-Solid-State Li-Ion Batteries, *J. Electrochem. Soc.* **165**, A1857 (2018).
- [18] D. Lin, Y. Liu, and Y. Cui, Reviving the lithium metal anode for high-energy batteries, *Nat. Nanotech.* **12**, 194 (2017).
- [19] Y. Guo, H. Li, and T. Zhai, Reviving Lithium-Metal Anodes for Next-Generation High-Energy Batteries, *Adv. Mater.* **29**, 1700007, 1700007 (2017).
- [20] G. Bucci, B. Talamini, A. Renuka Balakrishna, Y.-M. Chiang, and W. C. Carter, Mechanical instability of electrode-electrolyte interfaces in solid-state batteries, *Phys. Rev. Mater.* **2**, 105407 (2018).
- [21] F. Hao and D. Fang, Tailoring diffusion-induced stresses of core-shell nanotube electrodes in lithium-ion batteries, *J. Appl. Phys.* **113**, 013507 (2013).
- [22] R. J. Asaro and V. A. Lubarda, *Mechanics of Solids and Materials*. Cambridge University Press, New York (2006).
- [23] C. Monroe and J. Newman, The Impact of Elastic Deformation on Deposition Kinetics at Lithium/Polymer Interfaces, *J. Electrochem. Soc.* **152**, A396 (2005).
- [24] P. Barai, K. Higa, and V. Srinivasan, Impact of External Pressure and Electrolyte Transport Properties on Lithium Dendrite Growth, *J. Electrochem. Soc.* **165**, A2654 (2018).
- [25] X. Zhang, W. Shyy, and A. Marie Sastry, Numerical Simulation of Intercalation-Induced Stress in Li-Ion Battery Electrode Particles, *J. Electrochem. Soc.* **154**, A910 (2007).
- [26] K. Kumaresan, Y. Mikhaylik, and R. E. White, A Mathematical Model for a Lithium-Sulfur Cell, *J. Electrochem. Soc.* **155**, A576 (2008).
- [27] Y. Qi, L. G. Hector, C. James, and K. J. Kim, Lithium Concentration Dependent Elastic Properties of Battery Electrode Materials from First Principles Calculations, *J. Electrochem. Soc.* **161**, F3010 (2014).
- [28] A. Paolone, R. Cantelli, G. Rousse, and C. Masquelier, The charge order transition and elastic/anelastic properties of LiMn₂O₄, *J. Phys.: Condens. Matter* **15**, 457 (2003).
- [29] A. Sakuda, Y. Takigawa, K. Higashi, Evaluation of elastic modulus of Li₂S-P₂S₅ glassy solid electrolyte by ultrasonic sound velocity measurement and compression test, *J. Ceram. Soc. Japan* **121**, 946 (2013).
- [30] C. O'Rourke and B. J. Morgan, Interfacial strain effects on lithium diffusion pathways in the spinel solid electrolyte Li-doped MgAl₂O₄, *Phys. Rev. Mater.* **2**, 045403 (2018).

- [31] J. Wei, D. Ogawa, T. Fukumura, Y. Hirose, and T. Hasegawa, Epitaxial Strain-Controlled Ionic Conductivity in Li-Ion Solid Electrolyte $\text{Li}_{0.33}\text{La}_{0.56}\text{TiO}_3$ Thin Films, *Cryst. Growth Des.* **15**, 2187 (2015).
- [32] A. M. Hafez, Y. Jiao, J. Shi, Y. Ma, D. Cao, Y. Liu, and H. Zhu, Stable Metal Anode enabled by Porous Lithium Foam with Superior Ion Accessibility, *Adv. Mater.* **30**, 1802156 (2018).
- [33] L. Porz *et al.*, Mechanism of Lithium Metal Penetration through Inorganic Solid Electrolytes, *Adv. Energy Mater.*, 1701003, 1701003 (2017).
- [34] T. L. Anderson, *Fracture Mechanics: Fundamentals and Applications*. Third Edition, CRC Press, Boca Raton (2005).
- [35] J. Wolfenstine, H. Jo, Y.-H. Cho, I. N. David, P. Askeland, E. D. Case, H. Kim, H. Choe, and J. Sakamoto, A preliminary investigation of fracture toughness of $\text{Li}_7\text{La}_3\text{Zr}_2\text{O}_{12}$ and its comparison to other solid Li-ionconductors, *Mater. Lett.* **96**, 117 (2013).
- [36] F. P. McGrogan, T. Swamy, S. R. Bishop, E. Eggleton, L. Porz, X. Chen, Y.-M. Chiang, and K. J. Van Vliet, Compliant Yet Brittle Mechanical Behavior of $\text{Li}_2\text{S}-\text{P}_2\text{S}_5$ Lithium-Ion-Conducting Solid Electrolyte, *Adv. Energy Mater.* **7**, 1602011, 1602011 (2017).
- [37] L. Gireaud, S. Grugeon, S. Laruelle, B. Yrieix, and J. M. Tarascon, Lithium metal stripping/plating mechanisms studies: A metallurgical approach, *Electrochem. Commun.* **8**, 1639 (2006).
- [38] A. Sharafi, C. G. Haslam, R. D. Kerns, J. Wolfenstine, and J. Sakamoto, Controlling and correlating the effect of grain size with the mechanical and electrochemical properties of $\text{Li}_7\text{La}_3\text{Zr}_2\text{O}_{12}$ solid-state electrolyte, *J. Mater. Chem. A* **5**, 21491 (2017).

FIGURES AND FIGURE CAPTIONS

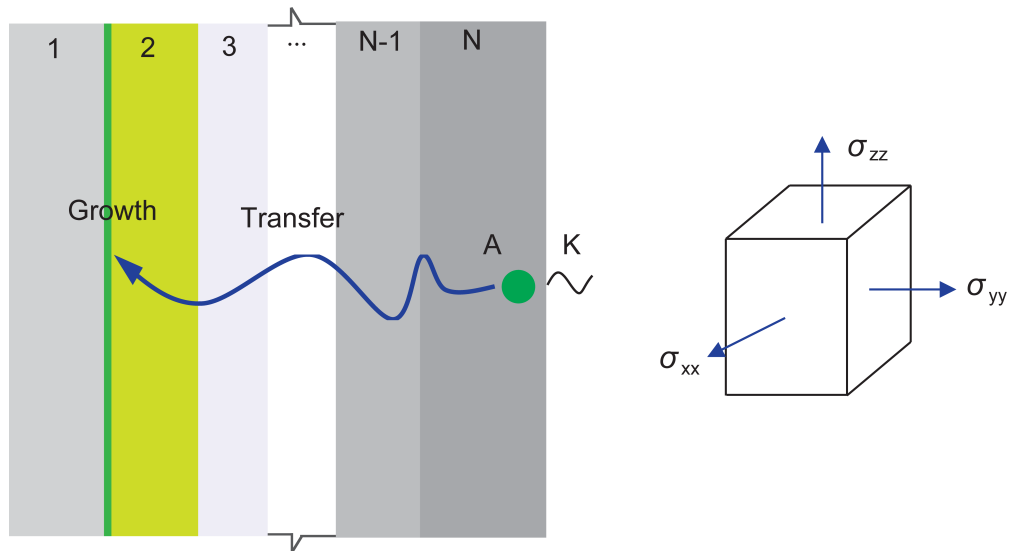


FIG. 1. Schematic of the interfacial growth in a layered structure, consisting of N layers. The green represents a newly formed layer (Layer 0). A is transferred from the reservoir of Layer N and deposited at the interface between Layer 1 and Layer 2. After the mass transfer, the N th layer contracts. K represents the external constraint stiffness applied to the layered structure. The right figure shows the stress state, with y -axis in the thickness direction (the horizontal direction).

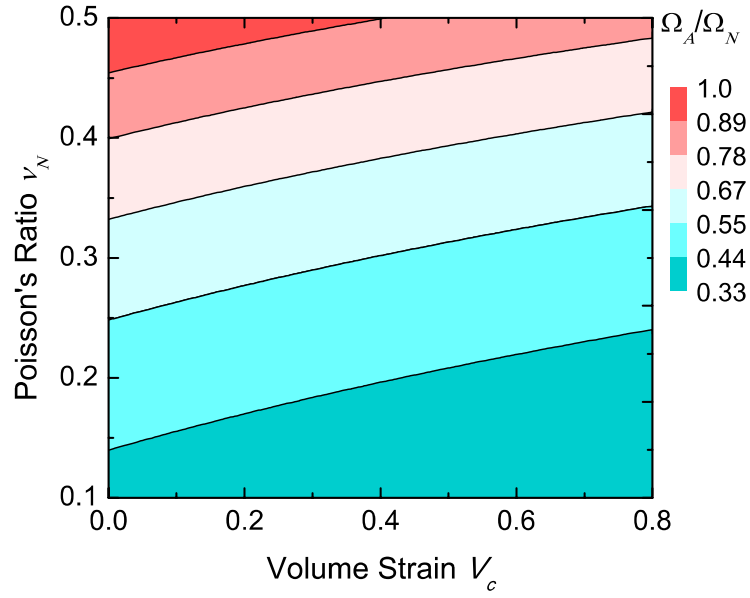


FIG. 2. In terms of the Poisson's ratio and volume strain of the N th layer, the calculated Ω_A/Ω_N for the condition that no stress is generated in the film thickness direction.

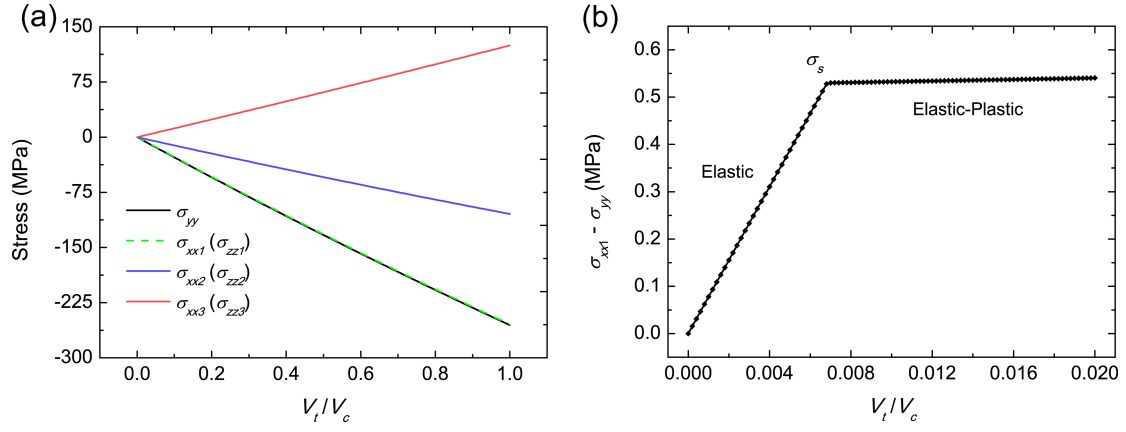


FIG. 3. Stress evolution during Li plating, where V_c is the maximum volume strain of the positive electrode and V_t is the volume strain of the positive electrode during plating. (a) Stresses of the positive electrode film, solid electrolyte separator, and Li metal. (b) Stress difference in Li metal.

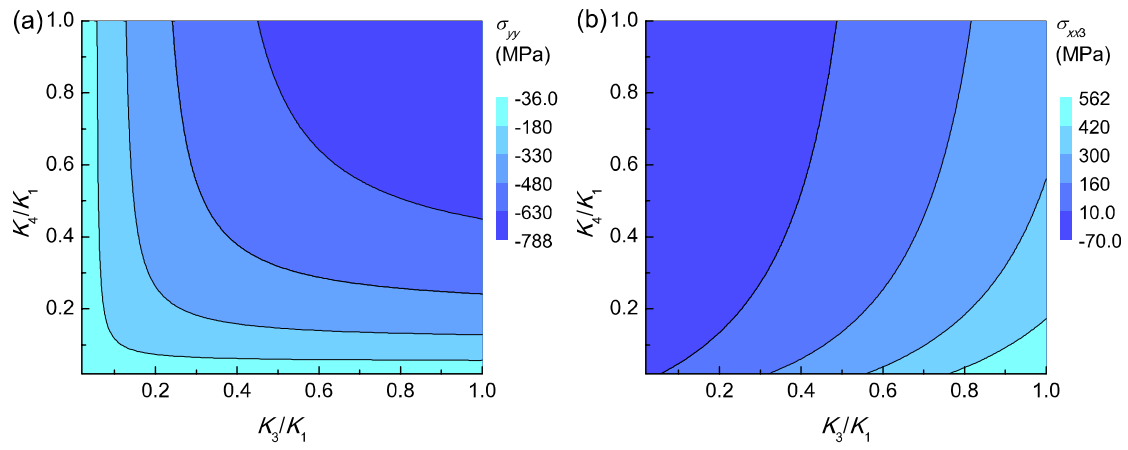


FIG. 4. In terms of K_3/K_1 and K_4/K_1 , σ_{yy} in the film thickness direction and σ_{xx3} in the positive electrode film.

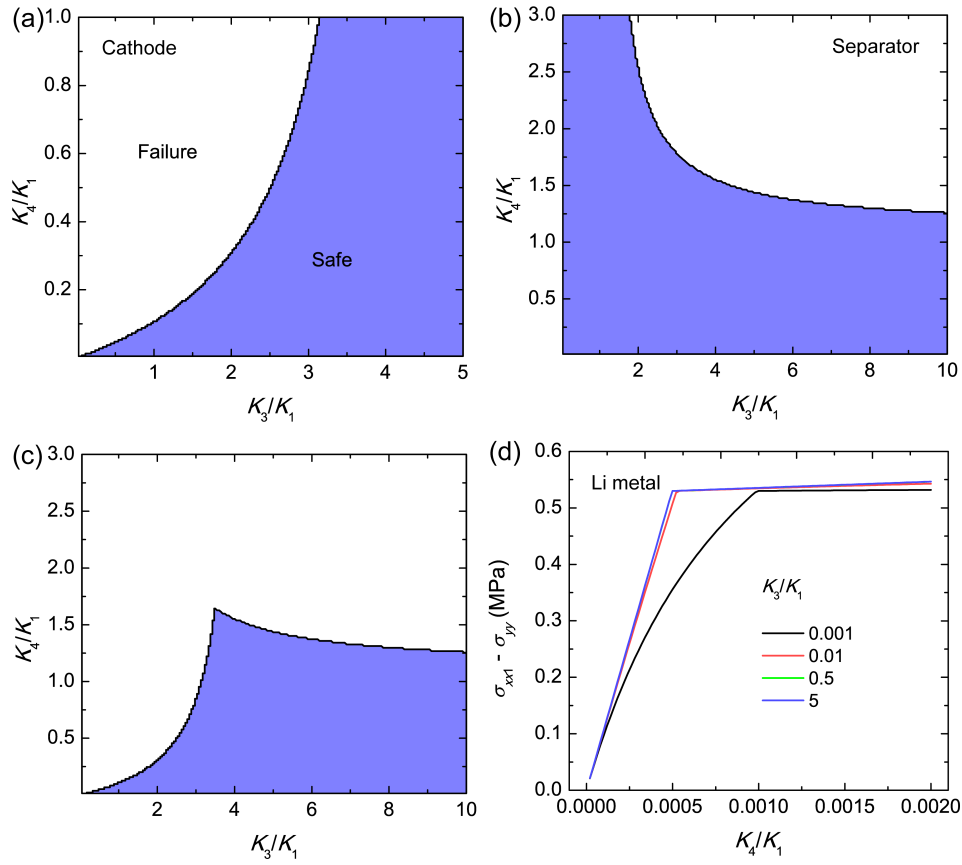


FIG. 5. For mechanical stability, the phase maps of (a) the positive electrode film and (b) solid electrolyte separator in terms of K_3/K_1 and K_4/K_1 . (c) Combined phase map for the positive electrode film and solid electrolyte separator. The blue is safe zone, and the white is failure zone. (d) Stress differences of Li metal with varying K_3/K_1 and K_4/K_1 .

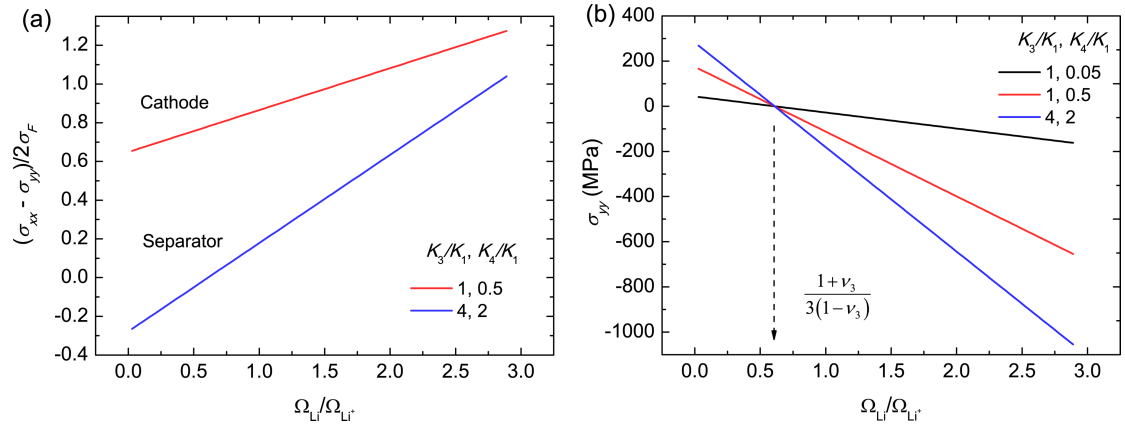


FIG. 6. Effect of Ω_{Li}/Ω_{Li+} on Li plating induced stress. (a) Stress for the positive electrode film and solid electrolyte separator. (b) Stress in the thickness direction.

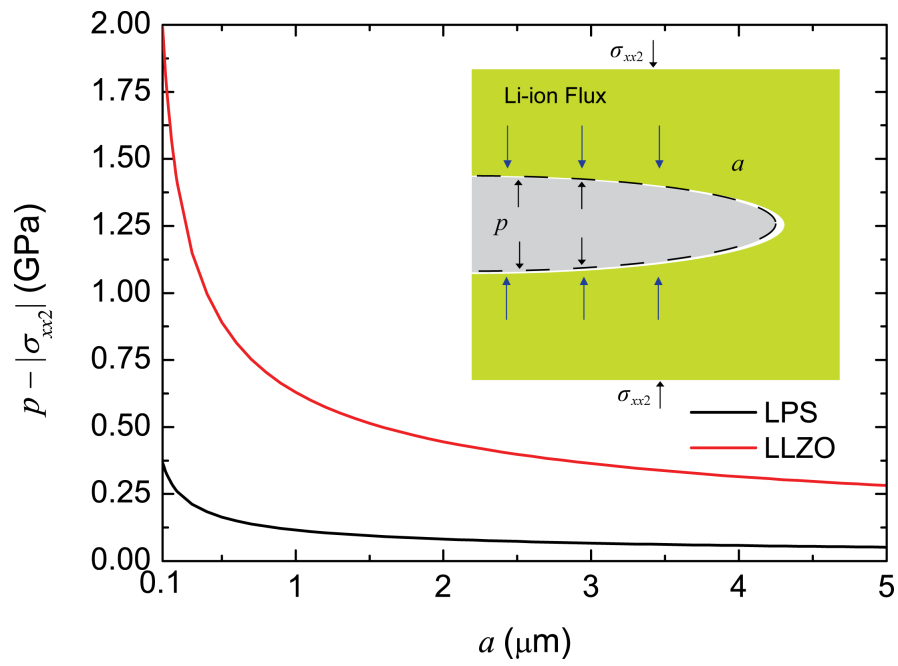


FIG. 7. For the solid electrolyte separators of LPS and LLZO, the critical stress, driving the crack propagation, depends on the length of surface flaw.